Palaeointensities of Oligocene and Miocene volcanic sections from Ethiopia: field behaviour during the Cainozoic

F. Lhuillier, V. P. Shcherbakov, V. V. Shcherbakova, S. Ostner, Gwenaël Hervé, N. Petersen

Geophysical Journal International

Geophys. J. Int. (2019) **216,** 1482–1494 doi: 10.1093/gji/ggy491

GJI Geomagnetism, rock magnetism and paleomagnetism

Palaeointensities of Oligocene and Miocene volcanic sections from Ethiopia: field behaviour during the Cainozoic

F. Lhuillier[1], V.P. Shcherbakov,[2,3] V.V. Shcherbakova,[2] S. Ostner,[1] G. Hervé[4] and N. Petersen[1]

[1]*Department of Earth and Environmental Sciences, Ludwig-Maximilians-Universität, Theresienstr. 41, 80333 Munich, Germany.*
E-mail: lhuillier@geophysik.uni-muenchen.de
[2]*GO Borok IPE RAS, v. Borok, Yaroslavl Oblast, 152742, Russia*
[3]*Institute of Geology and Petroleum Technologies, Kazan Federal University, Kremlyovskaya St. 4, Kazan 420008, Russia*
[4]*Aix Marseille Univ, CNRS, IRD, INRA, Coll France, CEREGE, 13545 Aix-en-Provence, France*

Accepted 2018 November 21. Received 2018 November 14; in original form 2018 August 30

SUMMARY

We conducted an absolute palaeointensity (API) survey on Ethiopian volcanics from Early Oligocene (Belessa section) and Middle Miocene (Debre Sina section). After a careful selection based on the reversibility of high-field thermomagnetic curves from samples yielding unambiguous palaeodirections, we restricted our analysis to five (resp. six) cooling units from Belessa (resp. Debre Sina), submitted to both Thellier and Wilson-style experiments. X-ray diffraction measurements and microscopical observations under reflected light gave us good confidence in the reliability of the remanence carriers of the Belessa basalts, with pseudobrookite exsolutions in titanomagnetite (TM) grains, synonymous of an advanced stage of high-temperature (i.e. deuteric) oxidation. In contrast, the Debre Sina trachybasalts may have been submitted to low-temperature (i.e. post-consolidation) alteration featured by granulation of TM grains and leading to a higher dispersion of API estimates. Compared to the 'world palaeointensity database', the lower dipole moment found in Ethiopia for the Early Oligocene ($30 \pm 8\,ZAm^2$) than the Middle Miocene ($65 \pm 20\,ZAm^2$) is compatible with a global increase of dipole strength from 30 Ma to present, and also suggestive of a dipole low during the Oligocene. This observation must however be treated with caution because of the over-representation of Plio-Pleistocene determinations in the global database and the partial correlation between dipole strength and number of palaeointensity determinations.

Key words: Magnetic field variations through time; Magnetic mineralogy and petrology; Palaeointensity; Palaeomagnetism; Rock and mineral magnetism.

1 INTRODUCTION

The Earth's magnetic field, generated by a dynamo process in the fluid outer core, is a dynamical object that can stochastically reverse its polarity. Since the Cretaceous Normal Superchron (84–124 Ma), the reversal frequency has increased from 1 to 5 times per Myr (e.g. Cande & Kent 1995; Ogg 2012), probably in response to a gradual change in the thermal conditions imposed by the mantle on the core (e.g. McFadden & Merrill 1984, 2000). The increase in the reversal rate can alternatively be interpreted in terms of two distinct segments with average rates of *ca.* $4\,Myr^{-1}$ for 0–40 Ma and *ca.* $1\,Myr^{-1}$ for 40–80 Ma (e.g. Gallet & Hulot 1997; Lowrie & Kent 2004), which either suggests rapid changes of the thermal conditions at the core–mantle boundary (e.g. Courtillot & Olson 2007) or a spontaneous nonlinear transition of the geodynamo state (e.g. Hulot & Gallet 2003).

In addition to its reversal frequency f, the field can be described by its rate of change during stable periods, called palaeosecular variation. This latter quantity is traditionally quantified by the standard angular deviation S of the virtual geomagnetic poles (also known as VGP scatter) calculated from a population of individual poles derived from several sites (e.g. Cox 1970; Cromwell *et al.* 2018), or when permitted by the relative variability ε_F in palaeointensity calculated from site-mean estimates (e.g. Cronin *et al.* 2001; Lhuillier *et al.* 2017). Both quantities are assumed to reflect the geodynamo state (e.g. McFadden *et al.* 1988; Lhuillier & Gilder 2013) and possibly correlate with f (e.g. Biggin *et al.* 2008; Lhuillier & Gilder 2013).

Finally, the field can be characterized by its absolute palaeointensity (API), most often recovered from stepwise Thellier-style experiments (e.g. Thellier & Thellier 1959; Shcherbakov & Shcherbakova 2001) or alternatively from continuous Wilson-style experiments

(e.g. Wilson 1961; Muxworthy 2010). Under the assumption of an axial dipole field, API determinations are usually converted into a virtual dipole moment (VDM, if the palaeoinclination of the observation is known) or a virtual axial dipole moment (VADM, if only the palaeolatitude of the observation is known), which are both independent of latitude and thus useful for global comparisons. Although API data suffer from inhomogeneous temporal sampling and large experimental uncertainties, recent analyses of the available databases suggest a loose negative correlation between dipole moment and reversal frequency (e.g. Tauxe 2006; Shcherbakov & Sycheva 2013) in agreement with numerical dynamo simulations (e.g. Aubert *et al.* 2010).

In this study, we focus on Ethiopian volcanics from Early Oligocene and Middle Miocene to better describe geomagnetic variability in this region over the past 30 Myr. In a companion paper (Lhuillier & Gilder 2019), we reported palaeomagnetic and K-Ar geochronological results of two piles of lava flows: a *ca.* 1-km-thick one (Belessa section) dated around 29–30 Ma and related to the Oligocene Afro–Arabian traps, as well as a *ca.* 700-m-thick one (Debre Sina section) emplaced during the Miocene in two periods around 10–11 and 14–15 Ma. Combining these new results with the available palaeomagnetic studies in the Afro–Arabian region, we argued that the VGP scatter was approximately 50 per cent higher during the Early Oligocene ($S = 14.2^{\circ}|^{15.4^{\circ}}_{13.2^{\circ}}$) or the Middle Miocene ($S = 15.0^{\circ}|^{16.5^{\circ}}_{13.8^{\circ}}$) than during the Plio-Pleistocene ($S = 9.7^{\circ}|^{10.5^{\circ}}_{9.0^{\circ}}$). As the reversal frequency f during the Early Oligocene is half that for the Plio-Pleistocene, it appears that S and f are uncorrelated in this near-equatorial region.

The aim of this paper is to complement the palaeodirectional results from the Belessa and Debre Sina sections with API determinations. Section 2 describes the sampling and magnetostratigraphy of the two investigated locations. Section 3 delineates the experimental methods employed for the determination of rock-magnetic properties and palaeointensities. Section 4 reports the results, laying the emphasis on how the success or failure of Thellier or Wilson-style experiments correlate with rock-magnetic properties or microscopical observations. Section 5 finally provides a discussion of the field behaviour in the Afro–Arabian region, supplemented by an analysis of the global API database during the Cainozoic.

2 SAMPLING AND MAGNETOSTRATIGRAPHY

2.1 Belessa section

The Belessa section, sampling the Early Oligocene Afro–Arabian traps, is located on the northwestern Ethiopian plateau close to the village of Belessa (12°24′07″N, 37°41′32″E, 2450 m), *ca.* 35 km southwest of Gondar (Figs 1a and b). As reported in Lhuillier & Gilder (2019), we sampled 69 sites over *ca.* 1 km of stratigraphic thickness, with an average stratigraphic spacing of 12 m for the bottom 800 m (63 sites). Each site corresponds to what we identified to be an independent lava flow and consists on average of eight samples preferably collected on two or three distinct locations on the bottom part of the flow. All sampled rocks are basalt, except phonolite on three sites that yielded uninterpretable palaeomagnetic results.

From the bottom to the top of the section, we identified 300 m of reverse polarity (R1) associated with chron C11r, 295 m of normal polarity (N1) associated with subchron C11n.2n, 55 m of reverse polarity (R2) associated with subchron C11n.1r, and the last 400 m of normal polarity (N2) associated with subchron C11n.1n (Fig. 2). This interpretation is in good agreement with previous studies on the history of the Afro–Arabian traps (Hofmann *et al.* 1997; Rochette *et al.* 1998; Coulié *et al.* 2003; Riisager *et al.* 2005) and consistent with the successful K-Ar age determination (29.57 ± 0.44 Ma) for site B68 at the top of the section (Lhuillier & Gilder 2019). It suggests that the whole section may have covered a time interval on the order of 1 Myr.

2.2 Debre Sina section

The Debre Sina section, sampling the Miocene Tarmaber-Megezez formation, is located on the northwestern Ethiopian plateau in the vicinity of the town of Debre Sina (9°51′00″N, 39°45′46″E, 2700 m), *ca.* 150 km northeast of Addis-Abeba (Figs 1b and c). As reported in Lhuillier & Gilder (2019), we sampled 59 sites over *ca.* 700 m of stratigraphic thickness with an average stratigraphic spacing of 19 m for the bottom 350 m (2600–2950 m, 18 sites) reducing to 9 m for the top 350 m (2950–3300 m, 41 sites). Each flow was sampled with the same strategy as for the Belessa section. The lower part of the section (2600–2950 m) is composed of rhyolitic ignimbrites, whereas the upper part (2950–3300 m) is more basic, with trachybasalts at the bottom and basaltic trachyandesites at the top.

K-Ar age determinations suggest a 4–5 Myr hiatus between the lower part of the section dated around 15.5–15 Ma and the upper part dated around 11–10.5 Ma (Lhuillier & Gilder 2019). The magnetostratigraphy only reveals normal polarities for the upper part, which suggests a time duration shorter than 300 kyr. The lower part is dominated by normal polarities with two reverse zones only represented by one point, which suggests a duration shorter than 1.2 Myr.

3 METHODS

We introduce in this section the methods employed in this study. We first conducted rock-magnetic measurements (Section 3.1) on two pilot samples of each site to determine the hypothetical domain structure and thermal stability. For sites showing both thermal and directional stability, we carried out additional rock-magnetic measurements, supplemented by X-ray structural analysis (Section 3.2) and reflected light microscopy (Section 3.3) on at least two samples per site to identify the remanence carriers and their oxidation stage. We finally conducted Wilson-style (Section 3.4) and Thellier-style (Section 3.5) experiments to determine APIs.

3.1 Rock-magnetic measurements

Rock-magnetic measurements were carried out at the University of Munich on 5-mm diameter cores. Hysteresis and backfield curves were made with a one-component Lakeshore Vibrating Sample Magnetometer (VSM). The hysteresis loops were corrected for the paramagnetic contribution by the slope above 0.5 T. From these measurements, standard hysteresis parameters—saturation magnetization (M_S), remanent saturation magnetization (M_{RS}), coercive force (H_C) and remanent coercive force (H_{CR})—were calculated and the hypothetical domain structure was estimated from the Day *et al.* (1977) plot using the ratios M_{RS}/M_S and H_{CR}/H_C. Continuous thermomagnetic curves $M_S(T)$ of the saturation magnetization (in a field of 200 mT) and $\chi(T)$ of the magnetic susceptibility (at a frequency of 3.4 Hz) were measured on a Variable Field Translation

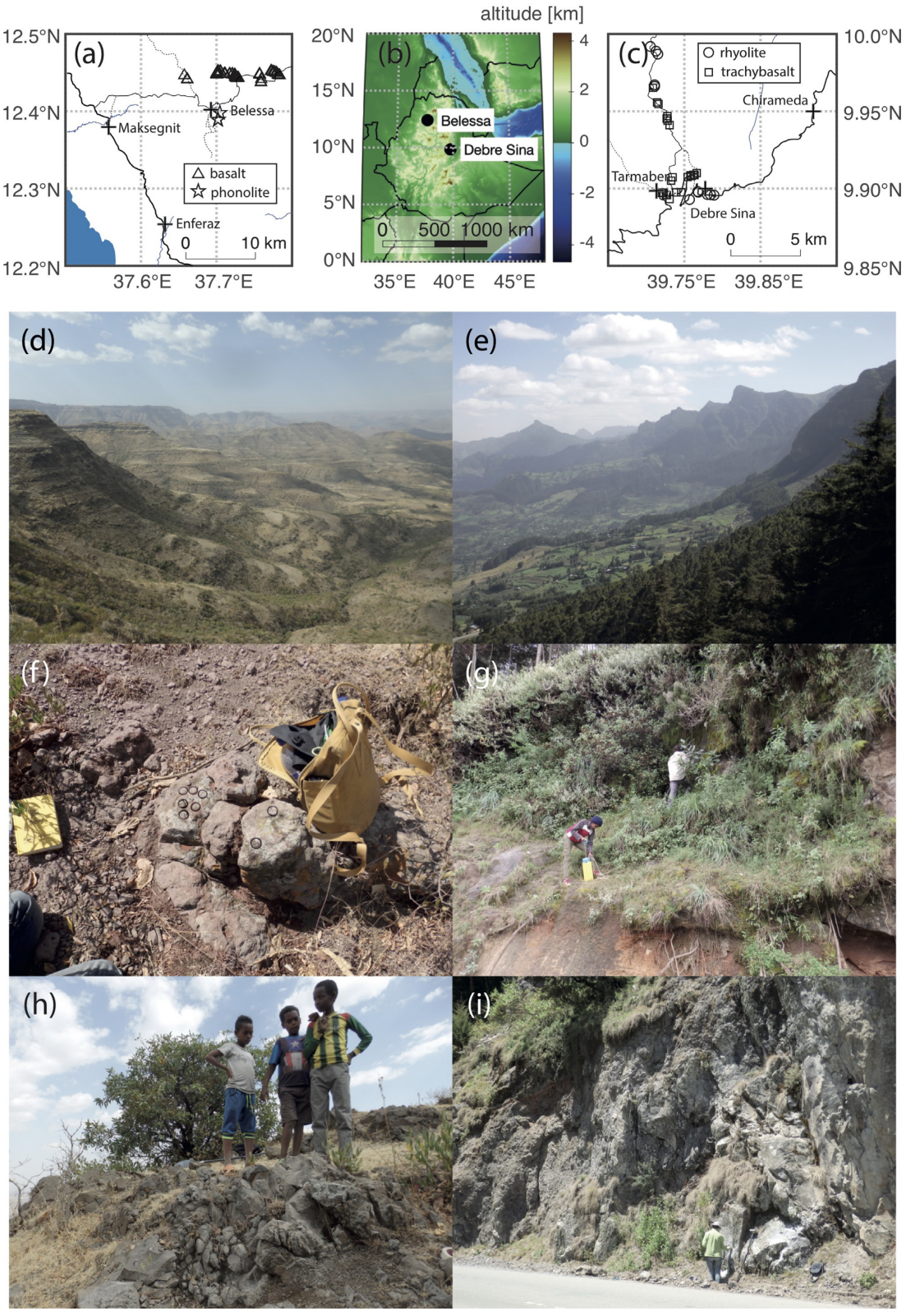

Figure 1. Location and field photographs of the investigated area. Panels (a) and (c): detailed maps of the Belessa (Early Oligocene) and Debre Sina (Middle Miocene) sections. Panel (b): digital elevation map (ETOPO1) of Ethiopia. Panels (d) and (e): overview of the Belessa and Debre Sina sections. Panels (f) and (h): sites B50 and B58 (basalts) from the Belessa section. Panels (g) and (i): sites M07 (ignimbrite) and M57 (trachybasalt) from the Debre Sina section.

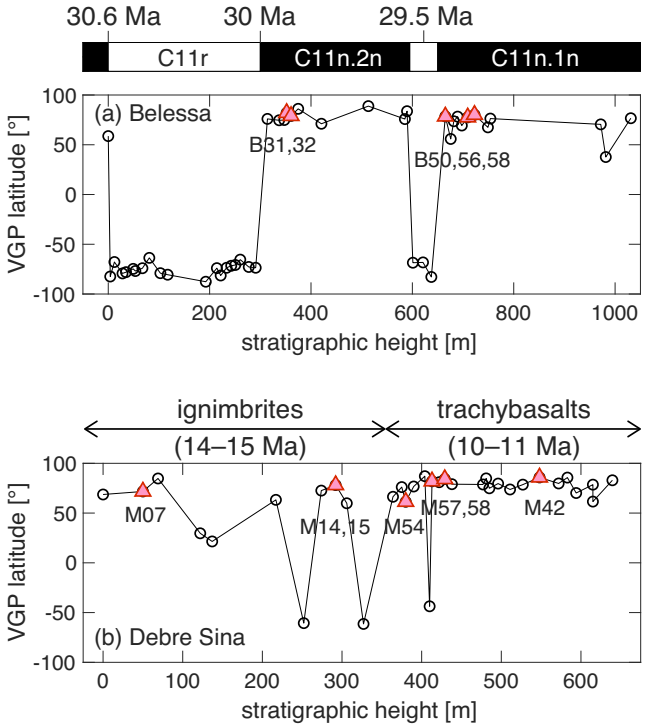

Figure 2. Magnetostratigraphy of the Belessa (Early Oligocene) and Debre Sina (Middle Miocene) sections. The red triangles represent the sites selected for absolute palaeointensity experiments. The geomagnetic polarity timescale stems from Ogg (2012).

Balance while heating in air from room temperature to 600 °C. The Curie points T_C were determined as the temperatures corresponding to the minima of the first derivative of the $M_S(T)$ or $\chi(T)$ curves (e.g. Fabian *et al.* 2013). To further assess the thermal stability of the samples, successive heating cycles $M_S^i(T)$ were measured for peak temperature $T_{max}^i = 100$, 200, 300, 400, 500 and 600 °C, still in an external magnetic field of 200 mT.

3.2 X-ray structural analysis

For 20 samples, the magnetic fraction, separated with a strong neodymium magnet, was subjected to X-ray structural analysis at the Geophysical Observatory of Borok with a STOE STADI multipurpose diffractometer (cobalt Kα_1 radiation) at room temperature. From the diffraction spectra, the ferrimagnetic phases were identified with their abundance and lattice constant a by comparison with the Crystallography Open Database (Gražulis *et al.* 2009, 2012). For a titanomagnetite $Fe_{3-x}Ti_xO_4$, we estimated the ulvöspinel content x and oxidation parameter z (fraction of original Fe^{2+} converted to Fe^{3+}) from the lattice constant a and the Curie point T_C by comparison with the Nishitani & Kono (1983) diagram.

3.3 Reflected light microscopy

For 30 palaeomagnetic cores, *ca.* 1-cm-high slices were prepared for reflected light microscopy. They were first manually polished with silicon carbide foils (FEPA P180 to P320 with average particle diameter from 80 to 40 μm) to flatten and smooth down the surface. They were then mechanically polished during 90–120 min with a 1 μm polycrystalline diamond paste, and 30 min with a 1/4 μm polycrystalline diamond paste. The polished sections were observed with a 50x oil objective mounted on a Leitz microscope. If necessary, we used a magnetic colloid, according to the Bitter (1932) technique, to better distinguish the magnetic contrasts within titanomagnetic grains.

3.4 Wilson-style palaeointensity experiments

The Wilson (1961) method compares a specimen's continuous thermal demagnetization of the natural remanent magnetization (NRM) with that of a full thermoremanent magnetization (TRM) induced in a known laboratory field B_{lab}. Over the chosen temperature range, the proportionality factor between NRM and TRM, multiplied by B_{lab}, provides an estimate B_{anc} of the API. Such experiments were conducted on 8.8-mm diameter cores at the Borok observatory using a custom-made, fully automated three-component VSM, which operates with a sensitivity of 10^{-8}Am^2 (e.g. Shcherbakova *et al.* 2012, 2014, 2017). To ascertain the robustness of the API determinations in the NRM–TRM diagram, useful parameters are: β, the relative standard error of the slope; f, the NRM fraction used for the fit; f_{res}, the residual TRM fraction at the origin.

3.5 Thellier-style palaeointensity experiments

The Thellier & Thellier (1959) method replaces in progressive stages a specimen's NRM with partial TRMs (pTRMs) induced in a known laboratory field B_{lab}. The experiments were carried out on 8.8-mm or 1-in diameter cores according to the double-heating protocol of Coe (1967) with pTRM checks, at the Borok observatory using the three-component VSM, and at the Munich University using an ASC-TD48 furnace together with an AGICO JR6 spinner magnetometer. For the Belessa section, a few specimens were additionally submitted to the Thellier-IZZI protocol (Tauxe & Staudigel 2004) at the Munich University using an Magnetic Measurements thermal demagnetiser (MMTD) furnace together with a 2G-Enterprises cryogenic magnetometer.

To assess the robustness of the API determinations, the following statistics were computed: n, the number of temperature steps used for the best-fit line on the Arai–Nagata diagram (Nagata *et al.* 1963); f, the NRM fraction used for the best-fit line on the Arai–Nagata diagram; β, the standard value of the slope normalized by its absolute value; q, the quality factor (Coe *et al.* 1978); *MAD*, the maximum angular deviation of the free-floating directional fits (Kirschvink 1980); α, the angular difference between the origin-anchored and free-floating best-fit directions; *DRAT*, the maximum difference ratio measured from pTRM checks (Selkin & Tauxe 2000); and *CDRAT*, the absolute value of the sum of the pTRM differences (Kissel & Laj 2004).

4 RESULTS

4.1 Rock-magnetic overview of the samples

For the two investigated sections, the bulk hysteresis properties shown in a Day plot (Figs 3a and b) mostly lie in the area usually associated with pseudo-single domain (PSD) behaviour. High-field thermomagnetic curves (Figs 3c and d) reveal a wide range of Curie temperatures from 100 to 600 °C and sometimes the coexistence of two ferrimagnetic phases, consistent with the presence of titanomagnetite. A few ignimbritic samples at the bottom of the Debre Sina section however did not fully demagnetize by heating to 600 °C, which suggests the presence of a small fraction of haematite.

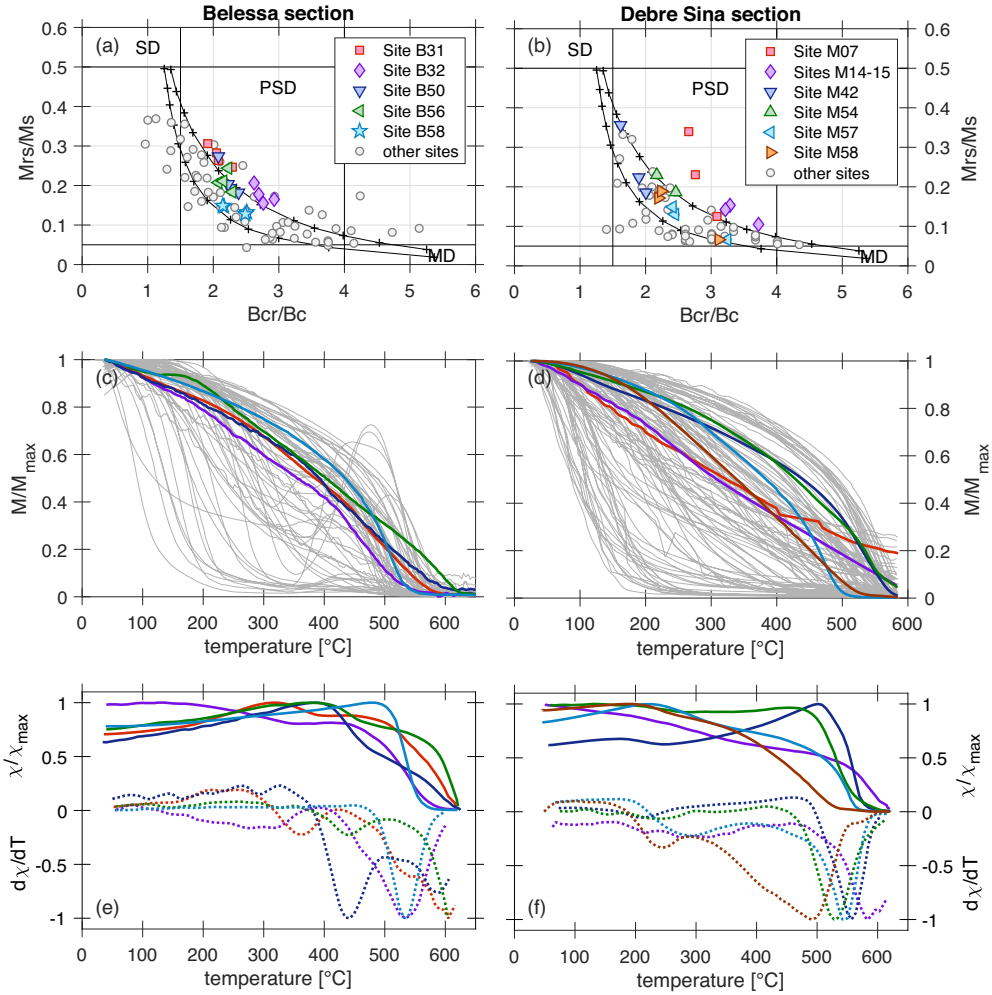

Figure 3. Rock-magnetic results for the Belessa section (left) and the Debre Sina section (right). Panels (a) and (b): Day plots. Panels (c) and (d): heating branches of $M_S(T)$ curves. Panels (e) and (f): heating branches of $\chi(T)$ curves with their first derivative to better identify the Curie points T_C. The coloured points/lines correspond to the sites selected for absolute palaeointensity determinations.

The Curie points of the main ferrimagnetic phase exceed 500 °C in 60 per cent of the cases for the Belessa section, only in 30 per cent of the cases for the Debre Sina section.

Among the sites that yielded successful palaeodirections (Lhuillier & Gilder 2019), we identified five flows at Belessa (B31, B32, B50, B56 and B58) and six flows at Debre Sina (M07, M14-15, M42, M54, M57 and M58) characterized by a reversible behaviour, to within 10 per cent, of the heating and cooling branches of the $M_S(T)$ curves up to 600 °C (Figs 4a and b and 5a and b). Only two sites (B56 and M54) are fully optimal for API experiments (e.g. Valet 2003), showing a single well-pronounced Curie temperature at 580–600 °C (Figs 3e and f, Table 3). The other sites are dominated by a high-temperature ($T_C = 500$ °C) titanomagnetite phase, coexisting with a lower temperature ($350 \leq T_C \leq 450$ °C for Belessa, $200 \leq T_C \leq 300$ °C for Debre Sina) titanomagnetite phase.

4.2 API results

For the six flows from Belessa, the demagnetization diagrams used for the directional analysis showed a secondary component removed by heating to 200 °C for sites B50 and B56 and to 400 °C for sites B31, B32 and B58. For the six flows from the Debre Sina section, the secondary component was easily removed by heating to 100–200 °C. For the two sections, the vector endpoint diagrams for all API samples produced an unambiguous unidirectional decay to the origin upon further demagnetization (Lhuillier & Gilder 2019).

We conducted on average ten Thellier and at least two Wilson experiments per site. The results were generally easier to interpret for the Belessa section, with the identification in most cases of a unique slope in the NRM–TRM diagrams of the Wilson (Figs 4c and d) and Thellier (Figs 4e and f) experiments. A caveat often found for the Wilson experiments is that the TRM did not perfectly go to the origin (Fig. 4d), which can be quantified by the y-intercept f_{res} of the linear fit. It suggests that a chemical transformation occurred during the TRM demagnetization and often led to aberrant API results. The palaeointensity results were in general less satisfactory for the Debre Sina section because of the presence of two distinct slopes in the NRM–TRM diagrams of the Wilson (Fig. 5c) and Thellier (Figs 5d and e) experiments. In the absence of a strong secondary component, we chose to interpret the slopes up to 400–500 °C for the Thellier experiments (Figs 5d and e), before chemical alteration indicated by negative pTRM checks occurred. The Wilson method, based on a full TRM, was not productive for the Debre Sina section because of the above-mentioned alteration occurring below

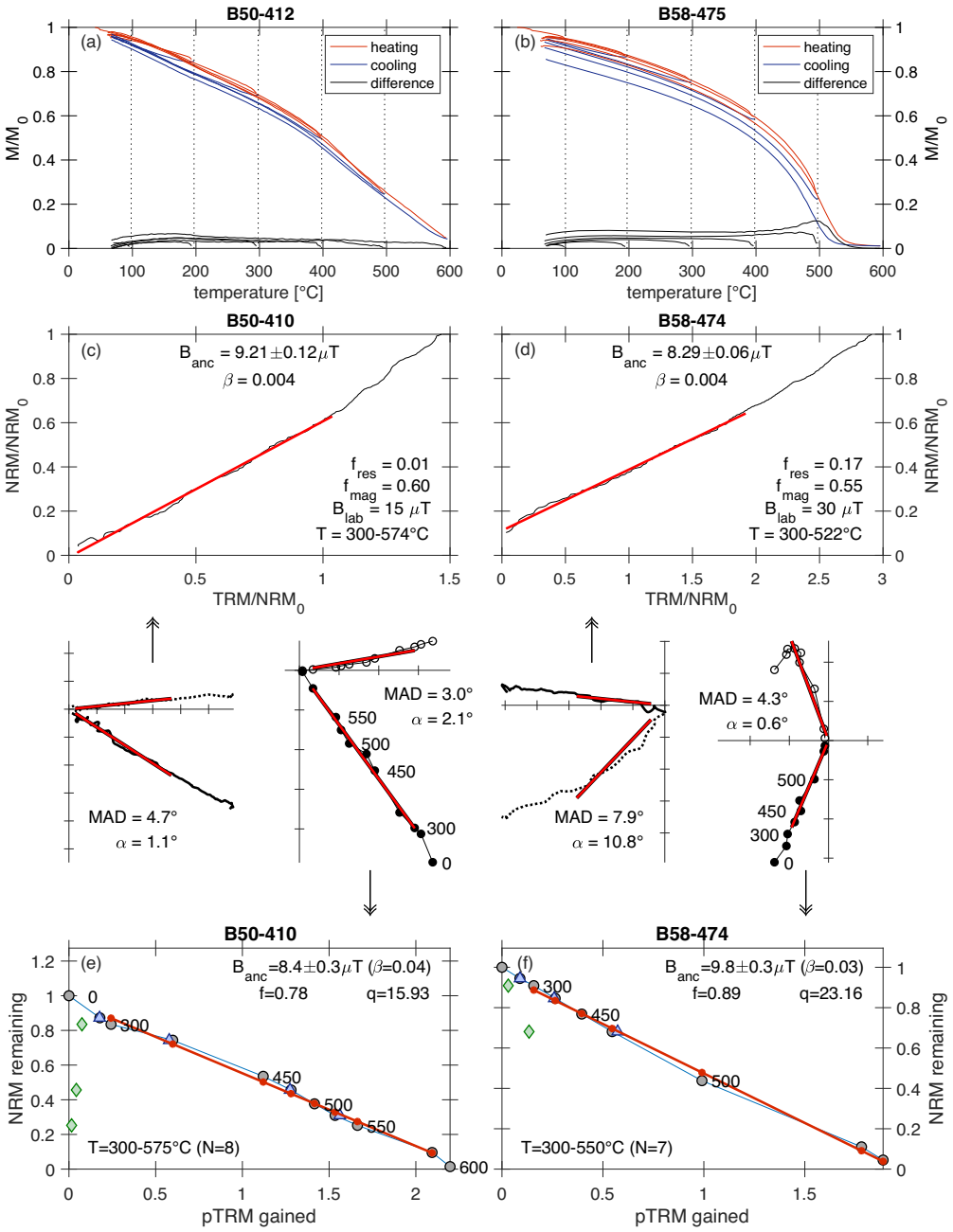

Figure 4. Typical absolute palaeointensity results for sites B50 (left) and B58 (right) of the Belessa section. Panels (a) and (b): iterative $M_S(T)$ curves to check thermal stability. Panels (c) and (d): NRM–TRM diagrams obtained from Wilson experiments. Panels (e) and (f): Arai–Nagata diagrams with pTRM checks (blue triangles) and pTRM-tail checks (green diamonds) obtained from Thellier experiments. The insets correspond to the associated vector endpoint diagrams. See Sections 3.4 and 3.5 for the definition of the statistics.

the Curie point, therefore these results are not included in further analyses.

The raw individual palaeointensity determinations are shown in Fig. 6(a) (see also Supporting Information Table S1). In essentials, the determinations from Debre Sina are twice higher but also twice more scattered than those from Belessa. Thellier and Wilson determinations are nearly indistinguishable for the Belessa section. For each of the two methods, we computed site-mean values (Table 1), which were then combined to produce time-averaged estimates at 29.5 Ma (from Sites B31, B32, B50, B56 and B58), at 14.5 Ma (from sites M07 and M14-15) and at 10.5 Ma (from sites M42, M54, M57 and M58).

We also produced a more conservative version of the estimates by applying the selection criteria reported in Table 2 on the individual determinations. The criteria were chosen slightly stricter than the PICRIT-03 criteria (Kissel & Laj 2004) for the Belessa section, more lenient for the Debre Sina section. Only seven specimens from Debre Sina would indeed pass the selection process if the criteria of Belessa were employed. It is however worth mentioning that the choice of the strict or lenient criteria for the Debre Sina section does not alter, to within 10 per cent, the site-mean averages. The application of the criteria satisfactorily led to a 25–50 per cent reduction of within-site dispersion for the Belessa section, whereas no clear improvement was observed for the Debre Sina section

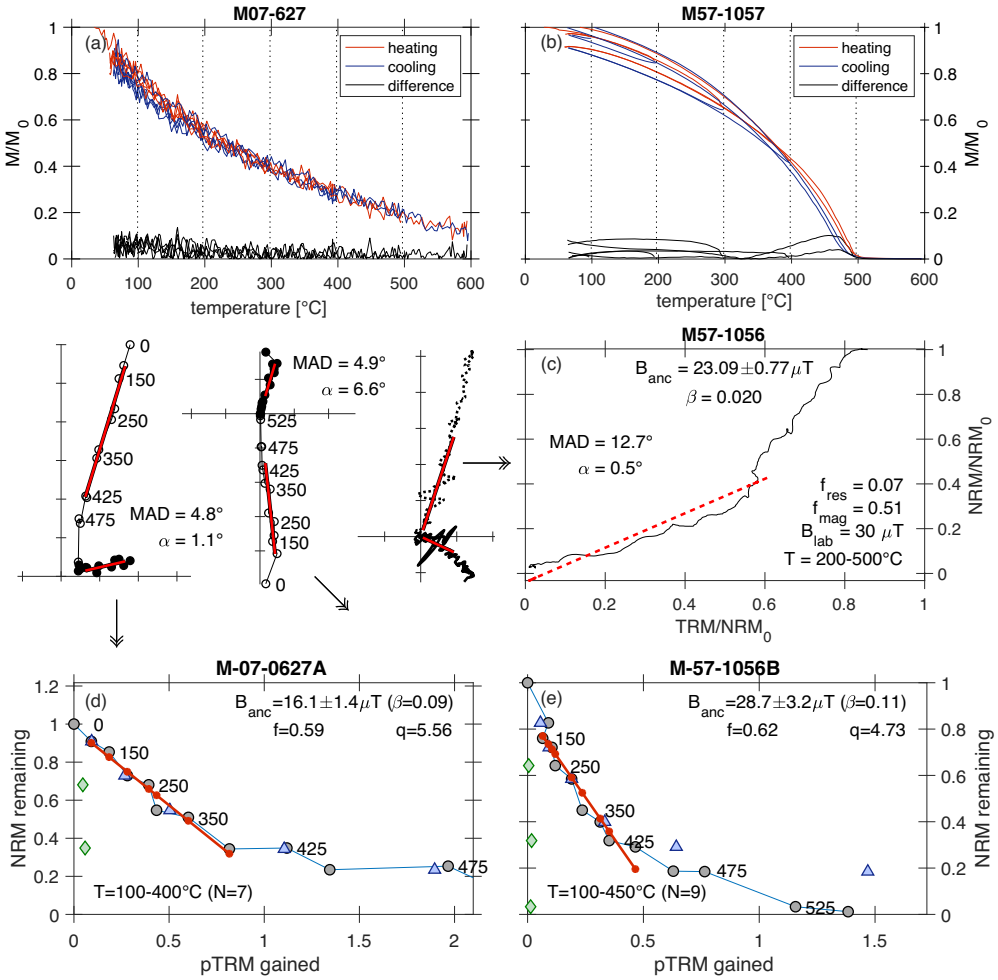

Figure 5. Typical absolute palaeointensity results for sites M07 (left) and M57 (right) of the Debre Sina section. Panels (a) and (b): iterative $M_S(T)$ curves to check thermal stability. Panel (c): NRM–TRM diagram obtained from a Wilson experiment; Panels (d) and (e): Arai-Nagata diagrams with pTRM checks (blue triangles) and pTRM-tail checks (green diamonds) obtained from Thellier experiments. The insets correspond to the associated vector endpoint diagrams. See Sections 3.4 and 3.5 for the definition of the statistics.

(Fig. 6, Table 1). Of note is that the Thellier and Wilson site-mean estimates remain nearly indistinguishable for sites B50 and B56, while the Wilson estimates are almost twice higher than the Thellier estimates for sites B31 and B32. It indicates that the remanence carriers exhibit a higher thermal instability for the specimens from sites B31 and B32 than those from sites B50 and B56. This is not visible from the Arai–Nagata diagrams but can be anticipated from the iterative $M_S(T)$ curves that are less reversible from 400–500 °C for the specimens from sites B31 and B32 than for those from sites B50 and B56. Thellier determinations should be in this case favoured because Wilson experiments are in principle only valid for remanence carriers that are thermally stable up to their Curie point. Since Wilson experiments are either indistinguishable from Thellier experiments or not trustworthy, we only used Thellier results in the rest of the study.

From the palaeointensities and palaeodirections (Lhuillier & Gilder 2019), we computed the VDMs according to standard definitions (e.g. Tauxe 2010). The Thellier-derived between-site time-averages are $3.0 \pm 0.8 \times 10^{22}$ Am^2 with $N = 48$ at 29.5 Ma, $4.8 \pm 0.6 \times 10^{22}$ Am^2 with $N = 5$ at 14.5 Ma and $7.8 \pm 1.3 \times 10^{22}$ Am^2 with $N = 22$ at 10.5 Ma (Table 1). This suggests an increase of the dipole moment from 30 to 10 Ma, an observation that will be discussed in Section 5.

4.3 Robustness of the remanence carriers

To assess the robustness of the remanence carriers and possibly explain the divergences between Thellier and Wilson determinations, we carried out X-ray structural analysis and reflected light microscopy on select specimens from the successful API results.

Crystallographic measurements were with some nuances in good agreement with thermomagnetic experiments (Table 3). For the Belessa section, two ferrimagnetic phases were usually detected, whereas a fraction of 15 to 45 per cent of weakly ferromagnetic hemoilmenite, probably as a result of the exsolution of the primary titanomagnetite, was also detected. We associated the titanomagnetite of largest lattice constant a with the lowest observed Curie point T_C, noting that the detection of a unique titanomagnetite phase for B56 partially disagrees with thermomagnetic curves. The use of the Nishitani & Kono (1983) diagram to estimate the ulvöspinel content x and oxidation parameter z revealed that the phase with $T_C \leq 450$ °C has more than 55 per cent of titanium whereas the titanium content in the phase with $T_C \geq 500$ °C does not exceed 35 per cent. All the titanomagnetite phases are moderately ($0.45 \leq z \leq 0.65$ for B56 and B58) to highly oxidized ($z \geq 0.85$ for B31, B32 and B50). For the Debre Sina section, the titanomagnetite phases detected by X-ray diffraction satisfactorily matched the Curie points observed in

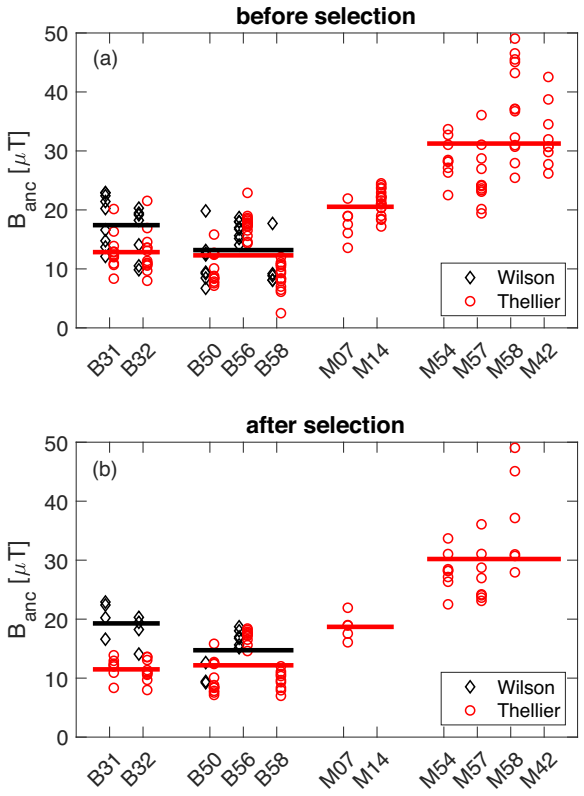

Figure 6. Summary of the individual absolute palaeointensity results before (panel a) and after (panel b) applying the selection criteria reported in Table 2.

the thermomagnetic curves. The titanomagnetites from sites M07, M14 and M54 are titanium-poor ($x \leq 0.20$) and moderately oxidized ($0.40 \leq z \leq 0.70$). The titanomagnetites from sites M42, M57 and M58 are titanium-rich ($0.55 \leq x \leq 0.70$) and moderately oxidized ($0.15 \leq z \leq 0.45$) for the low-T_C phase, titanium-poor ($0.20 \leq x \leq 0.25$) and slightly oxidized ($0.05 \leq z \leq 0.20$) for the high-T_C phase.

For the Belessa section, the polished sections from sites B50 and B56 showed a reddish matrix and titanomagnetite grains with systematic exsolution of pseudo-brookite and hemoilmenite (Fig. 7a). This corresponds to the most advanced stage of high-temperature oxidation, namely, the class VI defined by Ade-Hall *et al.* (1968a). Pseudo-brookite was unambiguously identified by its grey appearance with bluish tint, its weak anisotropy and its typical wavering intergrowth (e.g. Wilson & Haggery 1966; Wilson & Watkins 1967; Ramdohr 1969; Bowles *et al.* 2011). The magnetic colloid covered the titanomagnetite grains without clustering, which suggests that the magnetic poles are evenly distributed over the surface because the original titanomagnetite was exsolved in fine magnetite grains. In contrast, the polished sections from site B58 showed primary ilmenite lamellae typical of a tholeiitic basalt, and titanomagnetite grains systematically filled with fine ilmenite lamellae only visible in the presence of a magnetic colloid (Fig. 7b). This corresponds to an intermediate stage of high-temperature oxidation, namely, the class III of Ade-Hall *et al.* (1968a). Shrinkage cracks were possibly observed on some titanomagnetite grains (Fig. 7b), which suggests that low-temperature oxidation may have also occurred (e.g. Petersen & Vali 1987). Sites B31 and B32 finally showed titanomagnetite grains without visible intergrowths in 75 per cent of the cases (class I of Ade-Hall *et al.* 1968a) and with exsolution of pseudo-brookite and hemoilmenite in 25 per cent of the cases (class VI of Ade-Hall *et al.* 1968a). Based on these observations, sites B50 and B56 with an advanced stage of high-temperature oxidation would be the most appropriate for API experiments; site B58 would be the most questionable for API experiments because of possible signs of low-temperature oxidation; sites B31 and B32 are partially satisfactory with only one quarter of the titanomagnetite grains showing an advanced stage of high-temperature oxidation.

For the Debre Sina section, the polished sections of the rhyolitic ignimbrites (sites M07 and M14–15) showed little abundant and usually small titanomagnetite grains. These grains exhibited no intergrowth (class I of Ade-Hall *et al.* 1968a) or scarcely visible ilmenite lamellae (Fig. 7c, class III of Ade-Hall *et al.* 1968a). In contrast, the polished sections of the trachybasalts (sites M42, M54, M57 and M58) showed in a systematic way titanomagnetite grains with a granular texture (Fig. 7d), which is usually interpreted as the signature of low-temperature alteration (e.g. Ade-Hall *et al.* 1968a; Ade-Hall 1969) and is assumed to be little favourable for API determinations (e.g. Ade-Hall *et al.* 1968b). Whereas the granular texture was emphasized when a magnetic colloid was applied, the 10–20 μm exsolution patterns did not appear to be magnetic, were moreover isotropic and are thus probably hemoilmenite. As a conclusion for the Debre Sina section, we speculate that the granulation of the titanomagnetite grains is responsible for the higher dispersion of the API determinations of the trachybasalts.

In summary, the remanence carriers of the Belessa basalts are mostly titanomagnetite grains with pseudo-brookite exsolution, synonymous of an advanced stage of deuteric oxidation. The remanence carriers of the Debre Sina trachybasalts are mostly granulated titanomagnetite grains suggestive a low-temperature oxidation, whereas those of the Debre Sina ignimbrites are titanomagnetite with scarcely visible ilmenite intergrowths.

5 DISCUSSION

5.1 Reliability of API determinations

Due to the low success rate of API experiments, a careful preselection of the samples—either by checking the thermal stability of the remanence carriers from $M_S(T)$ curves or examining the shape of NRM demagnetization diagrams—is generally highly profitable (e.g. Valet 2003). The reliability of Thellier-style determinations is then assessed by the use of statistical criteria to quantify technical aspects of the results (e.g. Selkin & Tauxe 2000; Kissel & Laj 2004; Biggin *et al.* 2007). As emphasized by Biggin & Paterson (2014), the context and more qualitative aspects—such as the age constraint, the nature of the remanence carriers or the reproducibility of the results—are as important as, if not more than, the technical criteria to judge the reliability of the average determinations.

For this study, the reversibility of the $M_S(T)$ curves was certainly a prerequisite, but not a sufficient condition to classify the reliability of the investigated cooling units. First, failures of the Wilson experiments for the whole Debre Sina section, presumably because of the more pronounced propensity of the samples to chemical alteration from 400–500° during the experiments, are not a proof that the Thellier experiments are unreliable but make the estimates from the Belessa section more favourable. Second, observations of opaques under reflected light provides greater confidence in the estimates from the Belessa section. Sites B50 and B56 are the most trustful with an unambiguous signature of deuteric oxidation in an advanced stage (pseudo-brookite exsolution in all titanomagnetite grains). On the contrary, the reliability of the trachybasalts from the upper part

Table 1. Site-mean absolute palaeointensity determinations (B_{anc}) with their standard deviation ($\sigma(B_{anc})$) and associated virtual dipole moment (VDM), before and after applying the selection criteria (Table 2). Slon, Slat, Alt and Age report the longitude, latitude, altitude and age of the site. The next column reports the palaeointensity method: T for Thellier, W for Wilson. The rows in italic correspond to the between-site time-averaged estimates. The Thellier results in bold are those retained for interpretation.

Site	Slon (°E)	Slat (°N)	Alt (m)	Age (Ma)	Method	*n*	B_{anc} (μT)	$\sigma(B_{anc})$ (μT)	VDM (10^{22}Am^2)	*n*	B_{anc} (μT)	$\sigma(B_{anc})$ (μT)	VDM (10^{22}Am^2)
Belessa section						**Before selection**				**After selection**			
B31	37.7242	12.4469	2100	29.8	T	11	13.0	3.1	3.3	7	11.8	1.8	3.0
B31				29.8	W	9	18.6	4.3	4.7	4	20.5	2.9	5.2
B32	37.7241	12.4474	2108	29.8	T	13	12.7	3.5	3.2	10	11.3	1.8	2.8
B32				29.8	W	7	15.9	4.4	4.0	4	18.0	2.8	4.5
B50	37.7004	12.4493	2369	29.3	T	12	10.0	2.7	2.5	12	10.0	2.7	2.5
B50				29.3	W	8	11.5	4.1	2.8	3	10.4	1.9	2.6
B56	37.7006	12.4480	2415	29.3	T	15	17.6	2.0	4.5	10	17.1	1.2	4.4
B56				29.3	W	8	16.7	1.6	4.3	6	16.9	1.4	4.4
B58	37.7008	12.4478	2433	29.3	T	14	8.6	2.5	2.2	9	9.6	1.6	2.5
B58				29.3	W	5	10.4	4.1	2.7	0	—	—	—
mean				**29.5**	T	65	12.4	3.4	3.2	**48**	**12.0**	**3.0**	**3.0**
mean				29.5	W	37	14.6	3.5	3.7	17	16.5	4.3	4.2
mean				29.5	T+W	102	13.5	3.5	3.4	65	14.0	4.1	3.6
Debre Sina section						**Before selection**				**After selection**			
M07	39.7672	9.8460	2637	14.5	T	6	17.8	2.9	4.6	5	18.7	2.2	4.8
M14-15	39.7305	9.9166	2879	14.5	T	19	21.4	2.0	5.5	0	—	—	—
mean				**14.5**	T	25	19.6	2.5	5.1	**5**	**18.7**	**2.2**	**4.8**
M54	39.7565	9.8588	2967	10.5	T	9	28.7	3.4	7.2	8	28.2	3.3	7.1
M57	39.7540	9.8585	3000	10.5	T	12	25.4	4.7	6.5	8	27.2	4.5	6.9
M58	39.7522	9.8575	3016	10.5	T	13	37.5	7.8	9.6	6	36.8	8.6	9.4
M42	39.7413	9.8551	3135	10.5	T	9	32.5	5.2	8.3	0	—	—	—
mean				**10.5**	T	43	31.0	5.2	7.9	**22**	**30.7**	**5.3**	**7.8**

Table 2. Selection criteria used in this study, to be compared with those of PICRIT-03 (Kissel & Laj 2004). See Sections 3.4 and 3.5 for the definition of the statistics.

Statistic	Belessa	Debre Sina	PICRIT-03
	Thellier experiments		
n	≥5	≥5	≥4
β	≤0.1	≤0.15	≤0.1
q	≥5	≥1	≥2
f	≥0.5	≥0.3	≥0.35
MAD	≤10°	≤10°	≤7°
α	≤10°	≤10°	≤15°
|*DRAT*|	≤10 %	≤15 %	≤7 %
|*CDRAT*|	≤10 %	≤15 %	≤10 %
	Wilson experiments		
β	≤0.01		
f	≥0.5		
f_{res}	≤0.1		
MAD	≤5°		
α	≤10°		

Table 3. Structural analysis of titanomagnetite phases: Curie point T_C (deduced from thermomagnetic experiments); volume fraction *f*; lattice constant *a*; ulvöspinel content *x* and oxidation parameter *z* (both deduced from Nishitani & Kono 1983). The second column represents the stratigraphic height from the bottom of the section.

Site (Specimen)	*h* (m)	T_C (°C)	*f*	*a* (Å)	*x*	*z*
Belessa section						
B31(248A)	352	380	0.76	8.37	0.80	0.90
		550	0.24	8.35	0.25	0.85
B32(258A)	361	350	0.44	8.38	0.85	0.85
		520	0.56	8.34	0.40	0.95
B50(409A)	665	440	0.78	8.37	0.55	0.85
		580	0.22	8.35	0.35	0.85
B56(460A)	711	610	1.00	8.35	0.05	0.65
B58(479A)	728	530	1.00	8.38	0.20	0.45
Debre Sina section						
M07(622A)	50	540	0.19	8.37	0.20	0.53
		610	0.81	8.34	0.05	0.68
M14(683A)	290	580	1.00	8.36	0.10	0.53
M54(1023B)	380	540	1.00	8.38	0.18	0.40
M57(1056A)	413	290	0.53	8.43	0.63	0.45
		480	0.25	8.41	0.25	0.20
		540	0.22	8.38		
M58(1059B)	429	225	0.64	8.45	0.70	0.40
		480	0.36	8.42	0.22	0.05
M42(921A)	548	240	0.75	8.46	0.55	0.15
		525	0.25	8.40	0.20	0.20

of the Debre Sina section is the most questionable due to the observation of granular exsolution of the titanomagnetite grains, which is usually ascribed to a secondary low-temperature oxidation process that may have altered the original NRM. This caveat is directly associated with a higher dispersion of the API results in comparison to those from the Belessa section. The higher palaeointensities of sites M54, M57 and M58, although they pass our lenient selection criteria, would thus need to be confirmed by other studies in the same area.

5.2 Field behaviour in the Afro–Arabian region

Only three studies reported API determinations in the Ethiopian area: two for the stratoid basalts across the Réunion event during the Plio-Pleistocene (Carlut *et al.* 1999; Ahn *et al.* 2016), and one

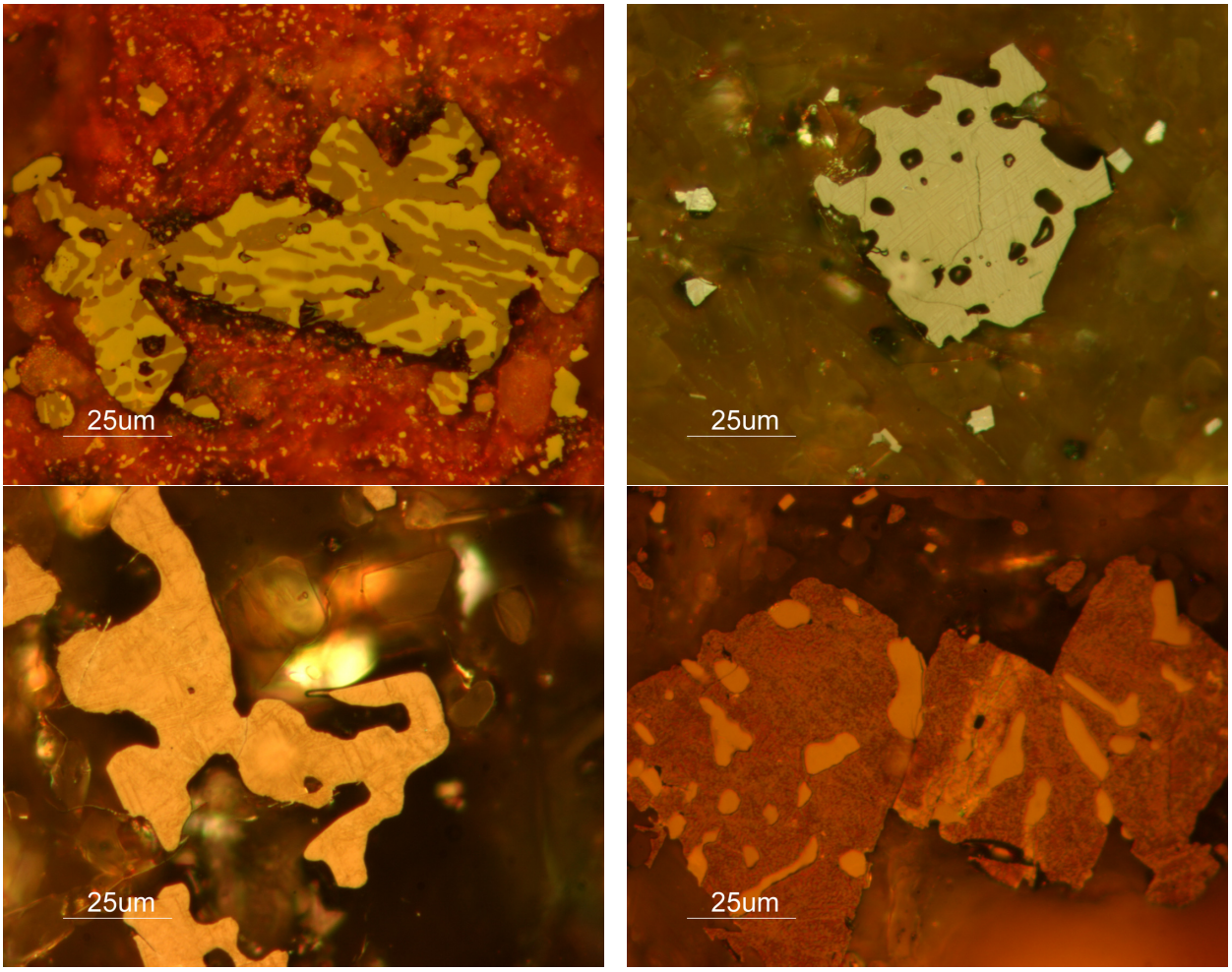

Figure 7. Typical microphotographs of titanomagnetite grains in the presence of a magnetic colloid: Sample B50-408 (top left) with pseudo-brookite (dark brown) and hemoilmenite (light brown) exsolutions; Sample B58-475 (top right) with fine ilmenite exsolution lamellae and possible shrinkage cracks; Sample M07-626 (bottom left) with hypothetical ilmenite exsolution lamellae; Sample M57-1057 (bottom right) with small-scale ($\sim 1\ \mu$m) granular exsolution of ilmenite and larger scale (10–20 μm) exsolution of hemoilmenite.

for the Afro–Arabian continental flood basalts during the Early Oligocene (Riisager *et al.* 1999).

For the Plio-Pleistocene, Carlut *et al.* (1999) and Ahn *et al.* (2016) reported average VDM values of $5.6 \pm 3.2 \times 10^{22}$ Am^2 (from 50 individual determinations and 20 cooling units) and $3.7 \pm 1.8 \times 10^{22}$ Am^2 (from 39 individual determinations and 12 cooling units) respectively. For the Middle Miocene, the Debre Sina section yielded an average VDM of $6.5 \pm 2.0 \times 10^{22}$ Am^2 (from 33 individual determinations and 5 cooling units). For the Early Oligocene Lima-Limo section, Riisager *et al.* (1999) determined VDMs of $7.2 \pm 2.5 \times 10^{22}$ Am^2 for chron C11r (~30.3 Ma) and of $4.2 \pm 1.1 \times 10^{22}$ Am^2 for C11n.1r (~29.5 Ma). In comparison, the Belessa section yielded VDMs of $2.9 \pm 0.1 \times 10^{22}$ Am^2 for chron C11n.2n (~29.8 Ma) and of $3.1 \pm 1.1 \times 10^{22}$ Am^2 for chron C11n.1n (~29.3 Ma). This leads to an average VDM 30 per cent lower for Belessa ($3.0 \pm 0.8 \times 10^{22}$ Am^2, from 48 individual determinations and 5 cooling units) than for Lima-Limo ($4.6 \pm 1.9 \times 10^{22}$ Am^2, from 17 individual determinations and 8 cooling units). We however note that the higher average VDM for Lima-Limo may be strongly biased by two cooling units (LL17 and LL19) with below average quality factors on the order of unit.

Whereas the VGP scatter was found to be 50 per cent higher during the Early Oligocene than during the Plio-Pleistocene in the Afro–Arabian region (Lhuillier & Gilder 2019), the associated API data available for this area do not reveal any clear trend (Fig. 8). This may mean that the two quantities are uncorrelated, as it seems to be the case between the VGP scatter and the reversal frequency in this area (Lhuillier & Gilder 2019). It may also mean that the number of independent API determinations in the Afro–Arabian region is not sufficient to derive a robust trend.

5.3 Field behaviour during the Cainozoic

To try to extract more robust trends, we compared our new data with the 'world palaeointensity database' (WPD) maintained by the Borok Geophysical Observatory (e.g. Shcherbakov *et al.* 2002; Shcherbakov & Sycheva 2006, 2013). This database includes all known published results of reconstructed dipole strength (in terms of VDM or VADM) obtained from eruptive or baked rocks. We focussed on the Cainozoic era and applied for each average estimate the selection criteria of Perrin & Shcherbakov (1997): (i) at least three individual determinations; (ii) a relative standard error lower

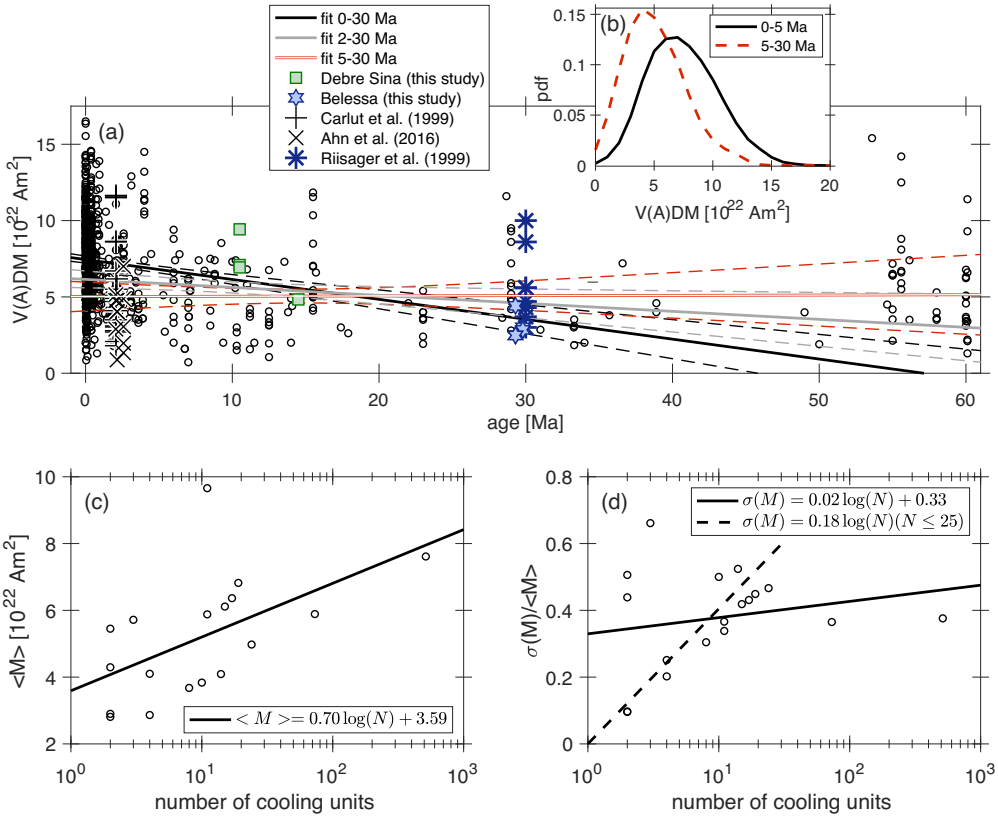

Figure 8. Analysis of the 'world palaeointensity database' (WPD) during the Cainozoic era. Panel (a): dipole strength as a function of age. Panel (b): probability density function (pdf) of dipole strength for the 0–5 and 5–30 Ma intervals. Panels (c) and (d): average value and relative standard error as a function of the number of determinations when data are grouped by 2-Myr windows.

than 15 per cent; (iii) the use of a check-point procedure. We moreover only considered the palaeointensity estimates obtained by the Thellier method and those occurring during the periods of stable polarity defined according to the authors' prescriptions. This gave us a set of 761 (out of 3209) average estimates for the investigated period (Fig. 8a).

A linear regression on the 0–30 Ma interval suggests an increase of the dipole strength from 3.5×10^{22} Am^2 at 30 Ma to 7.4×10^{22} Am^2 at present with a slope of 0.13×10^{22} Am^2 Myr^{-1}. We note that our estimates from Belessa and Debre Sina are in good agreement with this trend, whereas the Plio-Pleistocene data from Ethiopia (Carlut *et al.* 1999; Ahn *et al.* 2016) lie below the trend (Fig. 8a, black line). It is however important to bear in mind that 78 per cent (resp. 64 per cent) of the average estimates from the Cainozoic data set are younger than 5 Ma (resp. 1 Ma). According to Kolmogorov-Smirnov or Anderson-Darling tests, the probability that the 0–5 and 5–30 Ma subsets are taken from the same population is close to zero (Fig. 8b), suggesting a distinct behaviour during the Plio-Pleistocene. If the 0–5 Ma data are discarded, a linear regression on the 5–30 Ma interval reveals an absence of correlation between age and dipole strength (Fig. 8a, red line), which leads to overestimate by 40 per cent the Belessa determinations and underestimate by 30 per cent the Debre Sina determinations. If a linear regression is done from 2 to 30 Ma, an intermediate behaviour is found with a negative slope of *ca.* 0.05×10^{22} Am^2 Myr^{-1}, still showing a disagreement with Belessa and Debre Sina estimates.

Given the present state of the database, the two end-member scenarios—dipole low during the Oligocene on the one hand, constant dipole strength during the whole Cainozoic era on the other hand—are difficult to discriminate. As shown by Perrin & Shcherbakov (1997), the mean value $\langle M \rangle$ and standard deviation $\sigma(M)$ of the dipole strength over a given time window tend to correlate with the number N of palaeointensity determinations. For the Cainozoic era, an analysis by 2-Myr windows indicates that $\langle M \rangle$ linearly increases with $\log(N)$, by 230 per cent when N grows from 1 to 1000 (Fig. 8c). The relative standard error $\sigma(M)/\langle M \rangle$ seems to follow the same trend, with the difference that it may plateau at around 40 per cent from $N = 25$ (Fig. 8d). This suggests that a minimum of 25 independent determinations are probably desirable to yield a robust average of the dipole moment. As such a requirement is difficult to achieve for the whole Cainozoic unless three 20-Myr windows are considered, we cannot rule out that the dipole low during the Oligocene stems from an insufficient sampling during this period.

6 CONCLUSIONS

We determined the APIs of five Early Oligocene and six Middle Miocene cooling units from Central Ethiopia that, compared to the WPD for the Cainozoic era, lead to the following conclusions:

(1) The new determinations are compatible with an increase of the dipole moment from 30 Ma to present, thereby suggestive of a dipole low during the Oligocene.

(2) The alternative interpretation of a uniform dipole strength during the Cainozoic cannot be ruled out because of both the scarcity of the data prior to 5 Ma and the partial correlation between dipole strength and number of palaeointensity determinations.

From a rock-magnetic point of view, microscopical observations of titanomagnetite grains under reflected light indicate that:

(1) Wavering exsolution patterns of pseudo-brookite, traditionally associated with high-temperature oxidation, correlate with an enhanced thermal stability of the remanence carriers and consequently produce robust palaeointensity estimates.

(2) Granular exsolution with ilmenite grains of $\sim$1 μm diameter, presumably associated with low-temperature oxidation, produces on the contrary unsuitable material for Wilson experiments and dispersed Thellier palaeointensity results.

ACKNOWLEDGEMENTS

This study was supported by DFG grant LH55/4-1. VPS and VVS are thankful for the financial support from RFBR grant 17-05-00259 and state assignment of IPE RAS. GH was funded by ANR-CONACYT SVPIntMex project (ANR-15-CE31-0011-01) and by Campus France PRESTIGE program (PRESTIGE-2017-1-0002). We thank Geoffrey Cromwell and Anita Di Chiara for their constructive reviews, and Andy Biggin for editorial handling.

REFERENCES

Ade-Hall, J.M., 1969. Opaque petrology and the stability of natural remanent magnetism in basaltic rocks, *Geophys. J. Int.,* **18**(1), 93–107.

Ade-Hall, J.M., Khan, M.A., Dagley, P. & Wilson, R.L., 1968a. A detailed opaque petrological and magnetic investigation of a single tertiary lava flow from Skye, Scotland-I, *Geophys. J. Int.,* **16**(4), 375–388.

Ade-Hall, J.M., Khan, M.A., Dagley, P. & Wilson, R.L., 1968b. A detailed opaque petrological and magnetic investigation of a single tertiary lava flow from Skye, Scotland-III, *Geophys. J. Int.,* **16**(4), 401–415.

Ahn, H.-S., Kidane, T., Yamamoto, Y. & Otofuji, Y.I., 2016. Low geomagnetic field intensity in the Matuyama Chron: palaeomagnetic study of a lava sequence from Afar depression, East Africa, *Geophys. J. Int.,* **204**(1), 127–146.

Aubert, J., Tarduno, J.A. & Johnson, C.L., 2010. Observations and models of the long-term evolution of Earth's magnetic field, *Space Sci. Rev.,* **155,** 337–370.

Biggin, A.J. & Paterson, G.A., 2014. A new set of qualitative reliability criteria to aid inferences on palaeomagnetic dipole moment variations through geological time, *Front. Earth Sci.,* **2,** 1–9, 24.

Biggin, A.J., Perrin, M. & Dekkers, M.J., 2007. A reliable absolute palaeointensity determination obtained from a non-ideal recorder, *Earth planet. Sci. Lett.,* **257**(3-4), 545–563.

Biggin, A.J., van Hinsbergen, D.J.J., Langereis, C.G., Straathof, G.B. & Deenen, M.H.L., 2008. Geomagnetic secular variation in the Cretaceous Normal Superchron and in the Jurassic, *Phys. Earth planet. Inter.,* **169,** 3–19.

Bitter, F., 1932. Experiments on the nature of ferromagnetism, *Phys. Rev.,* **41**(4), 507–515.

Bowles, J.F.W., Deer, W.A., Howie, R.A., Vaughan, D.J. & Zussman, J., 2011. *Rock-Forming Minerals: Non-Silicates: Oxides, Hydroxides and Sulphides,* Geological Society.

Cande, S. & Kent, D.V., 1995. Revised calibration of the geomagnetic polarity timescale for Late Creataceous and Cenozoic, *J. geophys. Res.,* **100**(B4), 6093–6095.

Carlut, J., Valet, J.-P., Quidelleur, X., Courtillot, V., Kidane, T., Gallet, Y. & Gillot, P.-Y., 1999. Paleointensity across the Réunion event in Ethiopia, *Earth planet. Sci. Lett.,* **170**(1–2), 17–34.

Coe, R.S., 1967. The determination of paleo-intensities of the Earth's magnetic field with emphasis on mechanisms which could cause non-ideal behavior in Thellier's method, *J. Geomagn. Geoelec.,* **19**(3), 157–179.

Coe, R.S., Grommé, C.S. & Mankinen, E.A., 1978. Geomagnetic paleointensities from radiocarbon-dated lava flows on Hawaii and the question of the Pacific nondipole low, *J. geophys. Res.,* **83**(B4), 1740–1756.

Coulié, E., Quidelleur, X., Gillot, P.-Y., Courtillot, V., Lefèvre, J.C. & Chiesa, S., 2003. Comparative K–Ar and Ar/Ar dating of Ethiopian and Yemenite Oligocene volcanism: implications for timing and duration of the Ethiopian traps, *Earth planet. Sci. Lett.,* **206**(3–4), 477–492.

Courtillot, V. & Olson, P.L., 2007. Mantle plumes link magnetic superchrons to phanerozoic mass depletion events, *Earth planet. Sci. Lett.,* **260**(3-4), 495–504.

Cox, A., 1970. Latitude dependence of the angular dispersion of the geomagnetic field, *Geophys. J. Int.,* **20**(3), 253–269.

Cromwell, G., Johnson, C.L., Tauxe, L., Constable, C.G. & Jarboe, N.A., 2018. PSV10: a global data set for 0-10 Ma time-averaged field and paleosecular variation studies, *Geochem. Geophys. Geosyst.,* **57**(9), 839–26.

Cronin, M., Tauxe, L., Constable, C.G., Selkin, P.A. & Pick, T., 2001. Noise in the quiet zone, *Earth planet. Sci. Lett.,* **190**(1–2), 13–30.

Day, R., Fuller, M.D. & Schmidt, V.A., 1977. Hysteresis properties of titanomagnetites: grain-size and compositional dependence, *Phys. Earth planet. Inter.,* **13**(4), 260–267.

Fabian, K., Shcherbakov, V.P. & McEnroe, S.A., 2013. Measuring the Curie temperature, *Geochem. Geophys. Geosyst.,* **14**(4), 947–961.

Gallet, Y. & Hulot, G., 1997. Stationary and nonstationary behaviour within the geomagnetic polarity time scale, *Geophys. Res. Lett.,* **24**(15), 1875–1878.

Gražulis, S. *et al.*, 2009. Crystallography open fatabase – an open-access collection of crystal structures, *J. Appl. Crystallogr.,* **42**(4), 726–729.

Gražulis, S. *et al.*, 2012. Crystallography open database (COD): an open-access collection of crystal structures and platform for world-wide collaboration, *Nucleic Acids Res.,* **40**(D1), D420–D427.

Hofmann, C., Courtillot, V., Féraud, G., Rochette, P., Yirgu, G., Ketefo, E. & Pik, R., 1997. Timing of the Ethiopian flood basalt event and implications for plume birth and global change, *Nature,* **389**(6653), 838–841.

Hulot, G. & Gallet, Y., 2003. Do superchrons occur without any palaeomagnetic warning? *Earth planet. Sci. Lett.,* **210**(1-2), 191–201.

Kirschvink, J.L., 1980. The least-squares line and plane and the analysis of palaeomagnetic data, *Geophys. J. R. astr. Soc.,* **62**(3), 699–718.

Kissel, C. & Laj, C., 2004. Improvements in procedure and paleointensity selection criteria (PICRIT-03) for Thellier and Thellier determinations: application to Hawaiian basaltic long cores, *Phys. Earth planet. Inter.,* **147**(2-3), 155–169.

Lhuillier, F. & Gilder, S.A., 2013. Quantifying paleosecular variation: insights from numerical dynamo simulations, *Earth planet. Sci. Lett.,* **382,** 87–97.

Lhuillier, F. & Gilder, S.A., 2019. Palaeomagnetism and geochronology of Oligocene and Miocene volcanic sections from Ethiopia: geomagnetic variability in the Afro-Arabian region over the past 30 Ma, *Geophys. J. Int.,* **216**(2), 1466–1481.

Lhuillier, F., Shcherbakov, V.P., Gilder, S.A. & Hagstrum, J.T., 2017. Variability of the 0–3 Ma palaeomagnetic field observed from the Boring Volcanic Field of the Pacific Northwest, *Geophys. J. Int.,* **211**(1), 69–79.

Lowrie, W. & Kent, D.V., 2004. Geomagnetic polarity timescales and reversal frequency regimes, in *Timescales of the Paleomagnetic Field,* pp. 117–129, eds Channell, J.E.T., Kent, D.V., Lowrie, W. & Meert, J.G., AGU

McFadden, P.L. & Merrill, R.T., 1984. Lower mantle convection and geomagnetism, *J. geophys. Res.,* **89**(NB5), 3354–3362.

McFadden, P.L. & Merrill, R.T., 2000. Evolution of the geomagnetic reversal rate since 160 Ma: is the process continuous? *J. geophys. Res.,* **105**(B12), 28 455–28 460.

McFadden, P.L., Merrill, R.T. & McElhinny, M.W., 1988. Dipole/quadrupole modeling of paleosecular variation, *J. geophys. Res.,* **93**(B10), 11 583–11 588.

Muxworthy, A.R., 2010. Revisiting a domain-state independent method of palaeointensity determination, *Phys. Earth planet. Inter.,* **179**(1–2), 21–31.

Nagata, T., Arai, Y. & Momose, K., 1963. Secular variation of the geomagnetic total force during the last 5000 years, *J. geophys. Res.,* **68**(18), 5277–5281.

Nishitani, T. & Kono, M., 1983. Curie temperature and lattice constant of oxidized titanomagnetite, *Geophys. J. Int.,* **74**(1), 585–600.

Ogg, J.G., 2012. Geomagnetic polarity time scale, in *The Geologic Time Scale 2012,* pp. 85–113, eds Gradstein, F.M., Ogg, J.G., Schmitz, M.D. & Ogg, G.M., Elsevier

Perrin, M. & Shcherbakov, V., 1997. Paleointensity of the Earth's magnetic field for the past 400 Ma: evidence for a dipole structure during the Mesozoic Low, *J. Geomagn. Geoelectr.,* **49**(4), 601–614.

Petersen, N. & Vali, H., 1987. Observation of shrinkage cracks in ocean floor titanomagnetites, *Phys. Earth planet. Inter.,* **46**(1–3), 197–205.

Ramdohr, P., 1969. *The Ore Minerals and Their Intergrowths,* Pergamon Press.

Riisager, J., Perrin, M. & Rochette, P., 1999. Palaeointensity results from Ethiopian basalts: implications for the Oligocene geomagnetic field strength, *Geophys. J. Int.,* **138**(2), 590–596.

Riisager, P., Knight, K.B., Baker, J.A., Ukstins Peate, I., Al-Kadasi, M., Al-Subbary, A. & Renne, P.R., 2005. Paleomagnetism and 40Ar/39Ar geochronology of Yemeni Oligocene volcanics: implications for timing and duration of Afro-Arabian traps and geometry of the Oligocene paleomagnetic field, *Earth planet. Sci. Lett.,* **237**(3–4), 647–672.

Rochette, P. *et al.*, 1998. Magnetostratigraphy and timing of the Oligocene Ethiopian traps, *Earth planet. Sci. Lett.,* **164**(3-4), 497–510.

Selkin, P.A. & Tauxe, L., 2000. Long-term variations in palaeointensity, *Phil. Trans. R. Soc. Lond., A,* **358**(1768), 1065–1088.

Shcherbakov, V.P. & Shcherbakova, V.V., 2001. On the suitability of the Thellier method of palaeointensity determinations on pseudo-single-domain and multidomain grains, *Geophys. J. Int.,* **146**(1), 20–30.

Shcherbakov, V.P. & Sycheva, N.K., 2006. On the variation in the geomagnetic dipole over the geological history of the Earth, *Izv., Phys. Solid Earth,* **42**(3), 201–206.

Shcherbakov, V.P. & Sycheva, N.K., 2013. On the intensity of the geomagnetic field in the geological past, *Izv., Phys. Solid Earth,* **49**(5), 699–717.

Shcherbakov, V.P., Solodovnikov, G.M. & Sycheva, N.K., 2002. Variations in the geomagnetic dipole during the past 400 million years (volcanic rocks), *Izv., Phys. Solid Earth,* **38**(2), 113–119.

Shcherbakova, V.V., Bakhmutov, V.G., Shcherbakov, V.P., Zhidkov, G.V. & Shpyra, V.V., 2012. Palaeointensity and palaeomagnetic study of Cretaceous and Palaeocene rocks from Western Antarctica, *Geophys. J. Int.,* **189**(1), 204–228.

Shcherbakova, V.V., Shcherbakov, V.P., Zhidkov, G.V. & Lubnina, N.V., 2014. Palaeointensity determinations on rocks from Palaeoproterozoic dykes from the Kaapvaal Craton (South Africa), *Geophys. J. Int.,* **197**(3), 1371–1381.

Shcherbakova, V.V., Biggin, A.J., Veselovskiy, R.V., Shatsillo, A.V., Hawkins, L., Shcherbakov, V.P. & Zhidkov, G.V., 2017. Was the Devonian geomagnetic field dipolar or multipolar? Palaeointensity studies of Devonian igneous rocks from the Minusa Basin (Siberia) and the Kola Peninsula dykes, Russia, *Geophys. J. Int.,* **209**(2), 1265–1286.

Tauxe, L., 2006. Long-term trends in paleointensity: the contribution of DSDP/ODP submarine basaltic glass collections, *Phys. Earth planet. Inter.,* **156**(3-4), 223–241.

Tauxe, L., 2010. *Essentials of Paleomagnetism,* University of California Press.

Tauxe, L. & Staudigel, H., 2004. Strength of the geomagnetic field in the Cretaceous Normal Superchron: new data from submarine basaltic glass of the Troodos Ophiolite, *Geochem. Geophys. Geosyst.,* **5**(2), 1–16, Article Q02H06.

Thellier, E. & Thellier, O., 1959. Sur l'intensité du champ magnétique terrestre dans le passé historique et géologique, *Ann. Géophys.,* **15**(3), 285–376.

Valet, J.-P., 2003. Time variations in geomagnetic intensity, *Rev. Geophys.,* **41**(1), 1004.

Wilson, R.L., 1961. The thermal demagnetization of natural magnetic moments in rocks, *Geophys. J. Int.,* **5**(1), 45–58.

Wilson, R.L. & Haggery, S.E., 1966. Reversals of the Earth's magnetic field, *Endeavour,* **25,** 104–109.

Wilson, R.L. & Watkins, N.D., 1967. Correlation of petrology and natural magnetic polarity in Columbia Plateau basalts, *Geophys. J. R. astr. Soc.,* **12**(4), 405–424.

SUPPORTING INFORMATION

Supplementary data are available at *GJI* online.

Belessa_Thellier.zip
Belessa_Wilson.zip
DebreSina_Thellier.zip
DebreSina_Wilson.zip
SupplementaryTable.xls.zip

Please note: Oxford University Press is not responsible for the content or functionality of any supporting materials supplied by the authors. Any queries (other than missing material) should be directed to the corresponding author for the article.